Journal of Mines, Metals and Fuels, *71(12B): 73-85; 2023. DOI: 10.18311/jmmf/2023/45515*

Print ISSN : 0022-2755

Journal of Mines, Metals and Fuels

Contents available at: *www.informaticsjournals.com/index.php/jmmf*

Modelling Substrate Analysis for Remanufacturing: Investigating the Plasma Beam Remelting Process (PBRP) in Surface Modification of Additively Manufactured SS316L

N. Chethan Kumar and Suyog Jhavar*

School of Mechanical Engineering, VIT-AP University, Inavolu, Beside AP Secretariat, Amaravati - 522237, Andhra Pradesh, India; Suyog.jhavar@vitap.ac.in

Abstract

Additively manufactured components often exhibit inferior surface quality and mechanical anisotropy, necessitating additional post-production processing, which in turn raises both manufacturing costs and lead times. This study investigates the impact of modifying plasma power and scanning speed in the Plasma Beam Remelting Process (PBRP) on SS316L. This technique induces a rise in contact surface temperature, which subsequently alters the mechanical characteristics and surface roughness of the additively fabricated SS316L. Grain size refinement down to the sub-micron level was observed after PBRP. Finite Element Analysis (FEA) will be employed in this study to analyse temperature distribution and fluctuations in thermal zones using commercially available software. The interrelationship of various parameters will be explored to determine the optimal conditions necessary for effective surface modification. The temperature distribution in the x-direction was measured, and zonal area identification was conducted at varied scanning speeds. The effective area for reducing thermal stresses was projected to be the length of the Heat Treatment Effect Zone (HTEZ) as an extended zone. Plasma powers ranging from 300 to 340 W, coupled with scanning speeds between 63 and 90 mm/min, yielded the best results for processing. These preliminary findings indicate that the PBRP technique holds promising potential as a post-processing tool for modifying the surfaces of additively manufactured parts.

Keywords: *Finite Elements Analysis, Heat Treatment Effect Zone (HTEZ), Plasma Beam Remelting, Thermal Zonal Area*

1.0 Introduction

Metal Additive Manufacturing (MAM) has emerged as a promising substitute for traditional metal processing methods. It involves the continuous heating and cooling of successive material layers, facilitated by computerized control. Directed energy deposition and powder bed fusion represent two primary AM techniques distinguished by their energy source and feedstock delivery mechanisms. These methodologies encompass various approaches, as illustrated in Figure 1. Previous studies[1,2] have highlighted that internal characteristics such as microstructure, thermal stresses, and mechanical properties vary depending on the specific AM technique employed. Post-processing is an integral stage in Metal Additive Manufacturing (MAM), essential for refining the quality and functionality of fabricated parts. Techniques like Powder Bed Fusion (PBF), including Selective Laser Melting (SLM) and Electron Beam Melting (EBM), often necessitate post-processing steps such as support removal, heat treatment for stress relief and material enhancement, and surface finishing to achieve desired

---

Author for correspondence

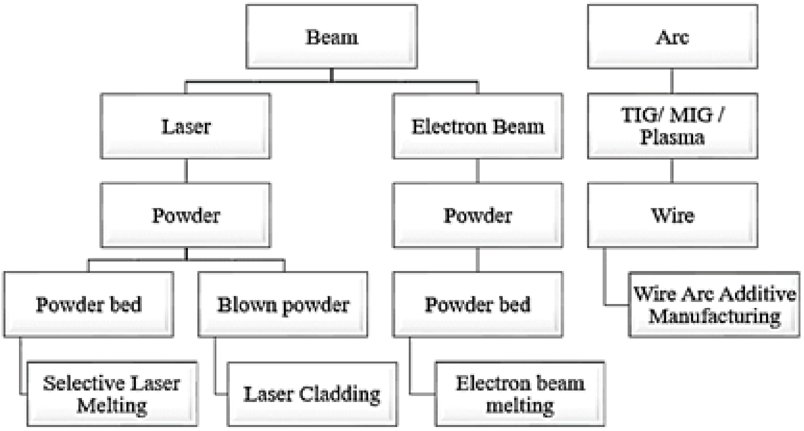

Figure 1. Metal additive manufacturing approaches based on the power source.

surface qualities and dimensional accuracies. Overall, post-processing remains pivotal in ensuring the integrity and performance of metal components produced through MAM, balancing manufacturing efficiency with quality assurance.

Figure 1 illustrates the different metal additive manufacturing techniques according to their power source. Surface modification by laser beam remelting has been the standard means in many studies due to its capability to provide optimal surface roughness values. For both SLM (Selective Laser Melting) and EBM (Electron Beam Melting) technologies, the average surface roughness value is between 10 and 30 µm. However, with WAAM (Wire Arc Additive Manufacturing) technology, the surface roughness value is significantly higher at 300 µm [3]. Surface polishing[4] is essential for achieving the desired finish in items produced through additive manufacturing. Several studies have been conducted on traditional contact-based methods such as machining, grinding, and polishing, which require longer processing times and can lead to excessive material wastage. To minimize these drawbacks, the implementation of improved surface polishing technologies is essential in order to achieve the desired level of finish. Surface modification techniques utilizing the same equipment used for additive manufacturing can now be achieved with the help of high-energy-beam technologies[5]. This innovative approach allows for automated polishing of a wide variety of materials without the need for physical contact. This method of polishing allows for surfaces to be refined to a level of precision that was previously impossible. Plasma beam[6] is a cost-effective and precise direct metal deposition technique that falls within the ASTM AM WAAM category. It offers a unique way of covering large areas in a short time period, resulting in significant cost savings and opening up new possibilities for application-based research in the future. With its open environment and micro-plasma technology, this process is both affordable and accurate.

Erik R. Denlinger *et al.*[7] applied Finite Element Modeling (FEM) to accurately forecast the distortion of AM components. They employed inactive element activation and adaptive coarsening in 3D thermoelastoplastic analysis to absorb moving energy, thus maintaining the material qualities of active components. As a proof-of-concept, they tested a 107-layer Ti-6Al-4V component deposited by Electron Beam Melting (EBM). R. Teimouri *et al.* investigated physics-based theoretical simulations aimed at predicting the evolution of surface roughness in components manufactured through Laser Powder Bed Fusion (LPBF) and subjected to subsequent burnishing processes. They address a critical gap by modelling the three-dimensional surface topography and roughness of LPBF-made components after burnishing, therefore improving our understanding of how burnishing influences surface quality in these components[8]. B. Zheng *et al.* proposed a hybrid additive manufacturing method, combining Laser Powder Bed Fusion (LPBF) with ultrafast laser machining, to improve dimensional accuracy and surface roughness. Parameters of ultrafast laser machining were investigated, showing enhanced surface quality compared to conventional LPBF. This approach presents promising prospects for advanced component manufacturing[9]. One potential research gap could be the need for further investigation into the impact of substrate properties, such as composition and surface finish, on the quality and performance of components produced through additive manufacturing processes. While studies have explored various aspects of additive manufacturing and post-processing techniques, there remains a gap in understanding how substrate characteristics influence the final outcome. This gap highlights the importance of conducting systematic studies to optimize substrate selection and preparation methods, ultimately enhancing the overall quality and functionality of additively manufactured parts.

To ensure accurate and smooth printed components, quality prediction at the design stage is essential. Computational analysis is the best approach for anticipating printed component quality. By running a thermal simulation with ANSYS 18.2, we can use the simulation data to adjust the printing settings and minimise surface roughness. This way, we can ensure that the intended design is accurately printed with minimal surface roughness. Thermal distribution histories are determined with 3D transient thermal analysis as the moving heat source is applied. Temperature gradients between the molten zone, Heat Treatment Effect Zone (HTEZ), and Heat Affected Zone (HAZ) are calculated using Temperature distribution results obtained from ANSYS temperature profile values. The length of the HTEZ is determined by the temperature gradient and the thermal properties of SS316L material. The authors investigate the benefits of utilising Wire Arc Additive Manufacturing (WAAM) with PBR to increase surface polish, subsurface qualities such as microstructure, microhardness and variations in laser interaction time and travel speed of the beam. By changing the Heat Treatment energy zonal areas and decreasing travel speed for 299W and 336W power of the beam, the insights were examined using a computational method for SS316L. Finally, to validate the simulation results, a comparison between the simulation findings and the experimental data was carried out.

2.0 Materials and Methodology

In this study, SS316L was chosen for its wide range of applications. The chemical characteristics of commonly available rolled materials were evaluated (see Table 1). To attain the required surface finish, the SS316L sample was cut to dimensions of 50 mm x 50 mm x 10 mm. The top surface underwent electro-discharge machining to achieve a roughness of 10 to 30 µm, aligning with the mean surface roughness of AM components. Additionally, the grain particle size was measured to be 80 ± 15 µm, and the micro-hardness value was recorded at 168 ± 12 HV before plasma remelting. Subsequently, the samples were cleaned with acetone, dried, and polished to achieve the desired material surface finish.

2.1 In-Lab Experimentation

The study employed in-house Plasma Additive Manufacturing equipment (PAM), featuring a computer-controlled wire feeder equipped, EWM Germany- a high-performance plasma power source[10], and a robust three-axis manipulator to ensure precise outcomes in welding and cutting tasks. Figure 2 depicts the experimental plasma arrangement, with Kay from Delft Spline Systems (The Netherlands) overseeing plasma power, scanning speed, and axis manipulation. During surface remelting, an argon barrier shielded the process from open air, while additional plasma shielding was provided by two cylinders of argon gas. Both shielding and pilot arc generation were set at 0.5 l/min. A 0.8-mm nozzle was consistently utilized across all experiments[11], each repeated three times, and the publication included the three best duplicates.

Table 1. SS316L's chemical configuration

C	Si	Mn	Cr	S	P	Mo	Ni	N	Fe
0.03	0.75	2.0	16.0	0.030	0.045	2.0	10	.10	Balance

Figure 2. Experimental setup for plasma remelting.

2.2 Methodology

Utilizing commercially available software Ansys 18.2, computational analysis was conducted to investigate the interaction line and travel speed of a beam with dimensions of 200 mm × 100 mm × 10 mm, focusing specifically on substrate properties. It was observed that decreasing the beam travel speed led to variations in the heat treatment zonal area (HTEZ), thereby increasing the laser interaction time with the work piece. Consequently, this prolonged interaction time resulted in an increased HTEZ and reduced thermal stresses. Based on prior reports, our preliminary experiments successfully established optimal plasma energy, beam travel speed, and Ar gas flow rate for effective shielding and plasma production, focusing exclusively on substrate properties. This ensures a safe and efficient plasma-based process. Remelting the material's surface to 0.5mm and solidifying it again with high plasma power can melt surface peaks and fill in troughs, resulting in a flatter, more uniform surface.

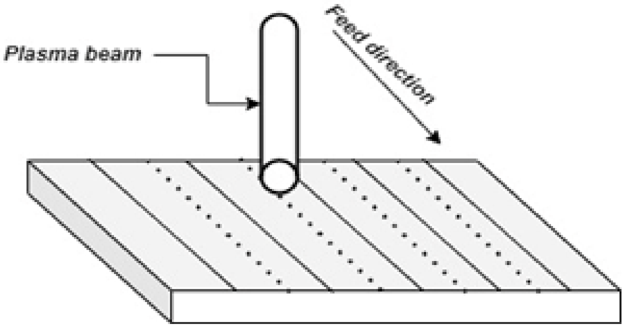

Figure 3. Plasma beam remelting method schematic.

Multiple-line scans with varied energy densities and scanning speeds determined the beam's impact on surface roughness. A single-pass approach was implemented to enhance surface and mechanical qualities, aiming for a smoother, consistent finish while minimizing procedure time. Time was identified as a critical factor influencing fabrication economy, guiding the selection of optimal settings for linear remelting. Horizontal surface remelting followed the determination of these settings. With a laser nozzle beam diameter of 0.8 mm and a step-over distance of 10 mm, overlapping passes were avoided in the plasma beam remelting method, ensuring consistency and accuracy in the welded region (see Figure 3 for a schematic).

3.0 Experimental and Computational Analysis Outcomes

Sixteen experiments conducted using plasma powers of 299 to 336 W and travel rates of 10 to 150 mm/min resulted in a drastic reduction of surface roughness by 60% compared to the traditional single-pass technique of PBR, with the optimum set of processing parameters. The heat required to melt the peaks and fill the valleys was also noted. The results indicate that PBR of SS316L can be effectively employed to dramatically decrease surface roughness in additively-manufactured products. Furthermore, the surface hardness was also enhanced by 75%, from 168±3.2 to 294.62±4.1 HV. Before remelting, the sample's average micro-hardness was at 168±3.2 HV. Hence, PBR has shown to improve the surface quality and mechanical properties of the sample.

3.1 Computational Analysis

Initiating the computational analysis, our study explores the impact of parameters on material characteristics and process performance, providing valuable insights for additive manufacturing methods. Table 2 presents the input process parameters that were considered during experimentation and the same parameters were used for computational analysis. The properties of the material SS316L are presented in Table 3. This provides insight into the material selection process and how the parameters chosen affect the overall performance of the computational analysis.

3.2 Requisite Moving Heat Source

Throughout the process of interaction of plasma beams during the deposition process, we mathematically modelled[12] the heat transfer to predict the thermal distribution of temperatures as given by Eq. 1

Temperature distribution (1)

$$\rho C \frac{\partial T}{\partial t} + \rho C u \nabla T = \nabla(\nabla T) + Q_g \quad (1)$$

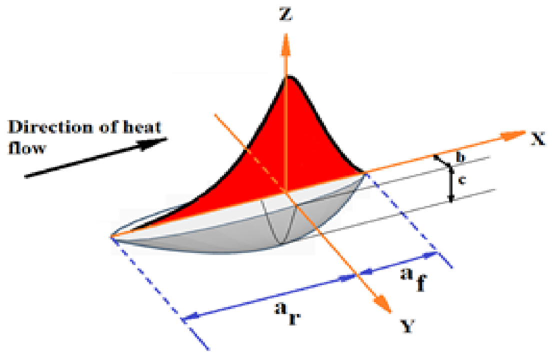

Figure 4. Goldak's moving double ellipsoidal heat source model[13].

Where is the density, C is specific heat and Qg is the Goldak's moving double ellipsoidal heat source model as shown in Figure 4.

The expression for determining the Qg is are as

Front heat source model

$$Q_{G1} = \frac{6\sqrt{3}\, Q_{heat\ source\ f_f}}{\pi\sqrt{\pi}\, a_f b c} e^{-3\left[\frac{(x-ut)^2}{a_f^2} + \frac{y^2}{b^2} + \frac{z^2}{c^2}\right]} \quad (2)$$

Table 2. Values of input process parameters

Input parameter (unit)	Values
Input Power (W)	299, 336
Beam travel speed (mm/min)	150, 130, 110, 90, 70, 50, 30, 10

Table 3. SS316L thermal properties

Property	**Values**
Thermal conductivity coefficient, λ	16.3×10^{-3} w/mm k
Thermal expansion coefficient, α	17.2×10^{-6}/k
Young's modules	190Gpa
Poisson's ratio	0.27
Isotropic thermal conductivity, K	14.6 Wm/K
Specific heat, C_p	110 J/kg K
Lattice parameter, m	0.3596 nm
Melting point	1400 °C
Boiling point	2861 °C
Latent heat of Fusion Lf	247 KJ/Kg
Latent heat of Vaporization Lv	6100 KJ/Kg

Rear heat source model

$$Q_{G2} = \frac{6\sqrt{3}\, Q_{heat\ source}\, f_f}{\pi\sqrt{\pi}\, a_r bc}\, e^{-3\left[\frac{(x-ut)^2}{a_r^2}+\frac{y^2}{b^2}+\frac{z^2}{c^2}\right]} \quad (3)$$

Where $Q_{heat\ source}$ is the power of plasma heat source generated for this study it taken to be 299W and 336W. Eq. 2 and Eq. 3 are the front heat source and rear heat source distributions. The values of af, ar, b, c, are computational investigation case-based values.

3.3 Analysis of Zonal Areas for Heat Treatment Effect Zone (HTEZ)

The component undergoes heating to elevated temperatures followed by rapid cooling during fabrication. This rapid thermal transition induces three-dimensional thermal stresses in all directions, forming distinct zonal areas denoted as Zx, Zy, and Zz, as represented by Equations 5, 6, and 7, respectively. This process enhances the strength and durability of the component. As depicted in Figure 5, various zones are generated during the deposition process. The plasma beam's high temperature melts the metal, creating a molten zone that remains liquid. Adjacent to this zone is the High-Temperature Effect Zone (HTEZ), where thermal stresses are mitigated due to the rapid heating and cooling process. Following is the Heat Affected Zone (HAZ), where the metal undergoes property alterations at elevated temperatures. Considering a moving heat source, these zones exhibit simultaneous movement.

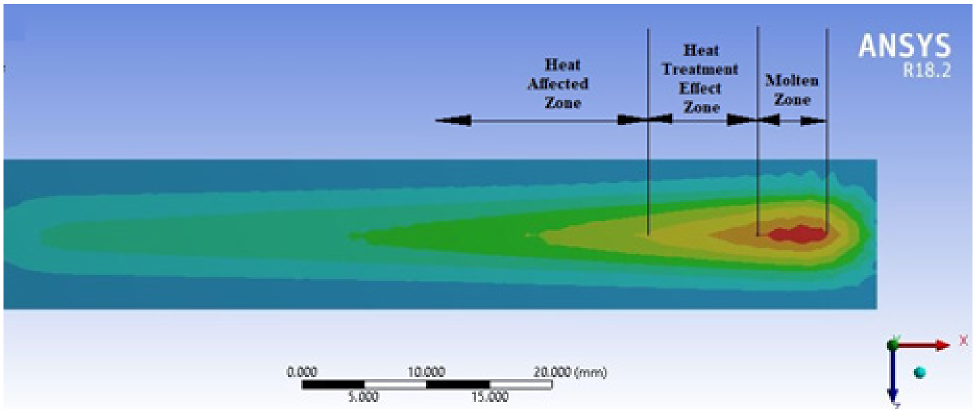

Figure 5. Various zones formed during the deposition process.

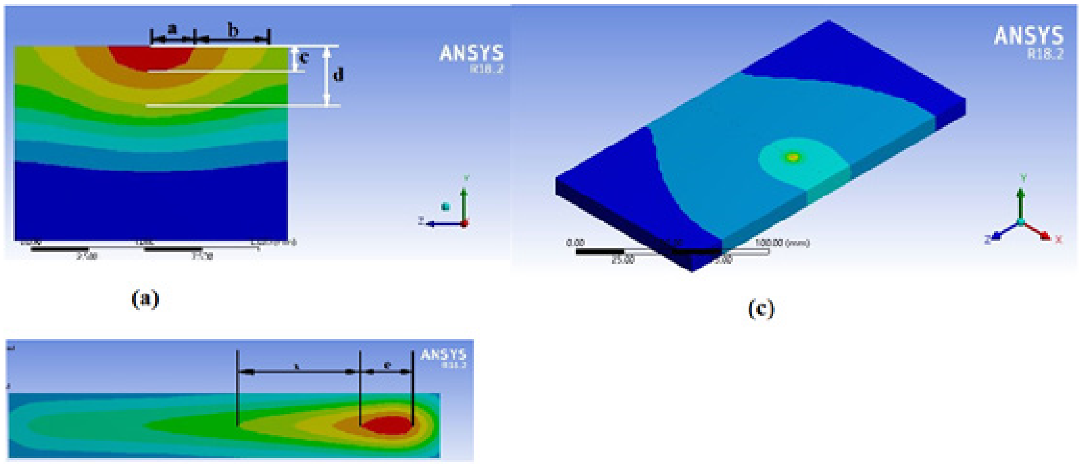

(a)

(c)

(b)

Figure 6. **(a)** HTEZ in ZY plane **(b)** HTEZ in XZ plane **(c)** HTEZ in Iso-plane of analysis of component.

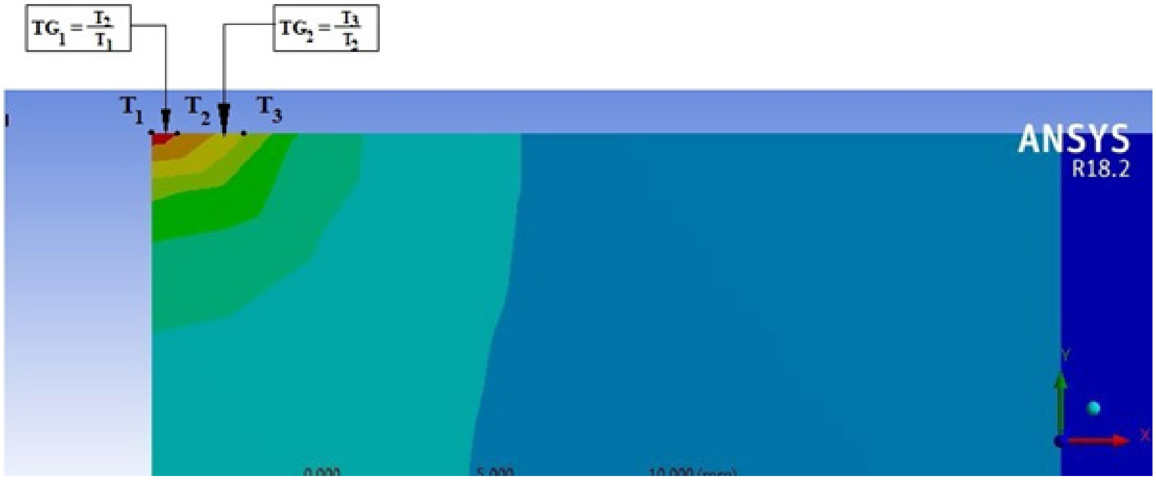

Figure 7. Temperature gradient calculation.

The length of HTEZ (x)[14] is expressed in terms of terms of temperature gradient (ΔT), thermal conductivity coefficient (λ), thermal expansion coefficient (α), lattice parameter (m), specific heat (C) and plasma beam interaction time (t) is calculated as using Eq. 4.

$$x = 1.22\sqrt{\frac{.\Delta T.\alpha.C.t}{m}} \tag{4}$$

$$\text{Where } \Delta T = TG_2 - TG_1 = \left|\left(\frac{T_3}{T_2}\right) - \left(\frac{T_2}{T_1}\right)\right|$$

HTEZ surfaces in all three direction is determined as
In x- direction Zonal area,

$$Z_x = (x+e)d - e.c \tag{5}$$

In y- direction Zonal area,

$$Z_y = 2(x+e)(a+b) - 2a.e \tag{6}$$

In x- direction Zonal area,

$$Z_z = 2[(a+b)d - a.c] \tag{7}$$

For calculating the length of time necessary for plasma beam contact, Eq. 8 is used. Additionally, the influence of beam width and plasma beam interaction duration on the various travel speeds of the beam is analysed to ensure an accurate calculation. By taking into consideration the plasma beam's interaction duration and the varying speeds of the beam, a precise estimate of the contact time can be determined.

$$\text{Plasma beam interaction time, } = \frac{d_b}{V}\ , \tag{8}$$

Where d_b diameter of the plasma beam = 0.8 mm , V = travel speed

The study is divided into three main sections. First, it introduces heat source models and provides transient temperature analyses to identify High Thermal Exchange Zones (HTEZ). Second, it presents previous experimental data regarding surface roughness. Finally, it correlates computational approaches to temperature distribution measurements with experimental results. Through this comprehensive approach, researchers can gain a better understanding of the relationship between heat transfer and surface roughness.

Latent heat of vaporization (Lv) is the amount of energy required to convert a given mass of material from a liquid to a gas at a constant temperature and pressure. Lv is calculated using the Eq. 9. Lv = Heat of Vaporization/Mass of material. The Heat of Vaporization, also known as enthalpy of vaporization, is the energy required to transform a certain amount of material from a liquid to a gas. By understanding the Heat of Vaporization, we can better understand the energy required for vaporization of a material and optimize the efficiency of industrial processes.

$$L_v = \frac{q}{m} \tag{9}$$

Where Lv = Latent heat of vaporization, KJ/Kg

$q = m \times C_p \times \nabla T$ = rate of heat transfer

m = Unit mass

∇T = Temperature difference

4.0 Results and Discussion

The temperature profile obtained from ANSYS was employed for precise determination of Temperature Gradient (TG) values, as depicted in Figure 7. Additionally, it served as the basis for computing the Heat Transfer Element Zone (HTEZ) length across 16 distinct experiments involving variations in power and travel speed, as detailed in Table 4. Table 5 presents the input power, scanning speed, temperature fluctuation, and latent heat of vaporization data.

After a thorough analysis of the various parameters, the graphical relationship between Travel Speed and Plasma Beam Interaction Time was plotted and discussed in the context of the substrate. As depicted in Graph 1, a decrease in the Travel Speed of the beam correlates with an increase in Plasma Beam Interaction Time, resulting in prolonged heating duration and subsequently an expansion in the length of the Heat Transfer Element Zone (HTEZ). For time durations corresponding to power levels of 299W and 336W, the variation ranged from 0.32 sec to 4.8 sec with Travel Speeds spanning from 150 mm/min to 10 mm/min. This increase in Interaction Time signifies enhanced heat absorption, leading to an augmentation in the length of Zonal Areas.

Graph 2 delves into the correlation between the Heat Transfer Expansion Zone (HTEZ) length and travel

Table 4. Computational values for laser interaction time, length of Heat Transfer Element Zone (HTEZ), and zonal areas

Trail No.	power (W)	travel speed (mm/min)	Plasma beam interaction time, sec	length of HTEZ - (x)	Zonal areas		
					x- direction	y- direction	z- direction
1	299	150	0.32	2.37	3.98	16.935	6.27
2	299	130	0.36	2.55	3.91	14.8	6.4
3	299	110	0.43	2.77	3.90	17.2	6.62
4	299	90	0.53	3.07	3.99	23.7	6.79
5	299	70	0.68	3.48	4.87	22.3	7.04
6	299	50	0.96	4.12	6.12	25.9	7.28
7	299	30	1.6	5.32	8.27	33.02	7.52
8	299	10	4.8	9.22	14.52	61.13	7.76
9	336	150	0.32	2.37	4.7	18.8	7.2
10	336	130	0.36	2.55	4.96	14.89	7.23
11	336	110	0.43	2.77	5.28	15.87	7.18
12	336	90	0.53	3.07	5.71	21.34	7.12
13	336	70	0.68	3.48	6.12	19.7	6.9
14	336	50	0.96	4.12	6.81	23.53	6.68
15	336	30	1.6	5.32	8.24	30.66	6.50
16	336	10	4.8	9.32	12.9	58.12	6.21

Table 5. Parameters: Input power, scanning speed, temperature variation, and latent heat of vaporization

Trail No.	power (W)	Scanning speed (mm/ min)	Temperatures			ΔT	Latent heat of vaporization (KJ/Kg)
			T1	T2	T3		
1	299	150	11644	10349	7758	0.14	4391.5
2	299	130	12514	11123	8341	0.14	4826.5
3	299	110	12490	11102	8327	0.14	4814.5
4	299	90	14142	12571	9429	0.14	5640.5
5	299	70	15315	13615	10214	0.14	6227
6	299	50	16699	14845	11139	0.14	6919
7	299	30	19211	17079	12815	0.14	8175
8	299	10	24583	21854	16396	0.14	10861
9	336	150	13081	11626	8715	0.14	5110
10	336	130	14060	12497	9371	0.14	5599.5
11	336	110	14032	12473	9354	0.14	5585.5
12	336	90	15888	14123	10593	0.14	6513.5
13	336	70	17207	15296	11475	0.14	7173
14	336	50	18761	16679	12514	0.14	7950
15	336	30	21584	19188	12001	0.14	9361.5
16	336	10	27617	24551	18419	0.14	12378

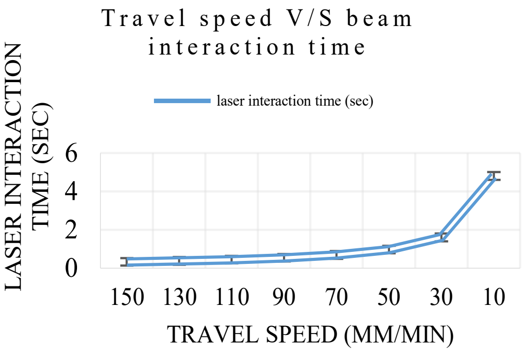

Graph 1. Relationship between travel speed and laser interaction time.

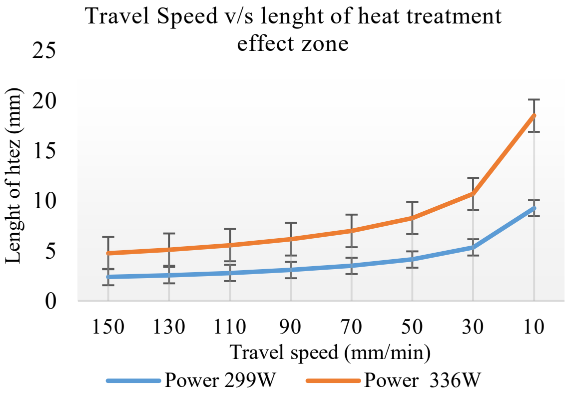

Graph 2. Correlation between travel speed and length of Heat Transfer Element Zone (HTEZ).

speed, a crucial parameter to consider given its impact on thermal stress relief. For a power of 299W, the HTEZ spans from 2.37 mm to 9.22 mm, while for 336W, it ranges from 2.37 mm to 9.23 mm, with scanning speeds ranging from 150 mm/min to 10 mm/min. This underscores the significance of optimizing travel speed to maximize

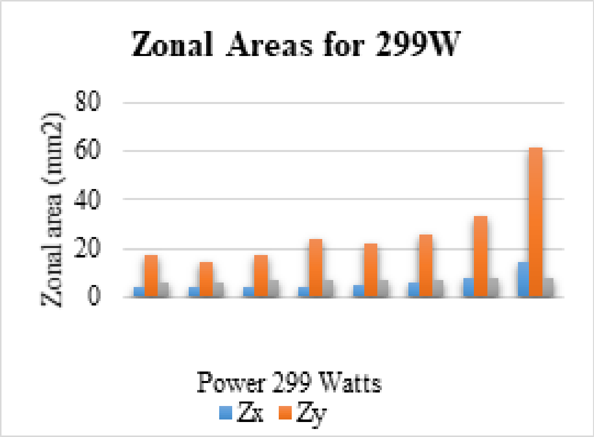

Graph 3. Relationship between travel speed and zonal areas in X, Y, and Z directions for 299W power.

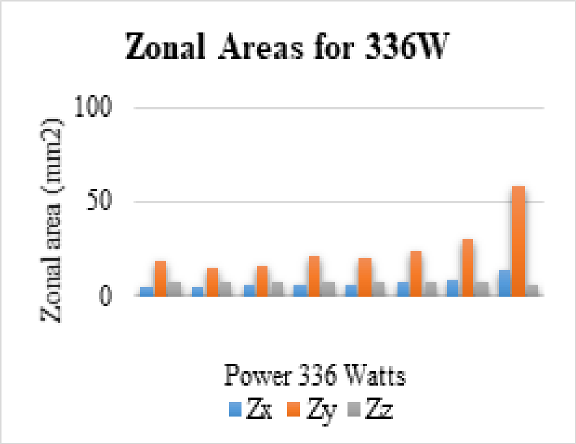

Graph 4. Correlation between travel speed and zonal areas in X, Y, and Z directions for 336W power.

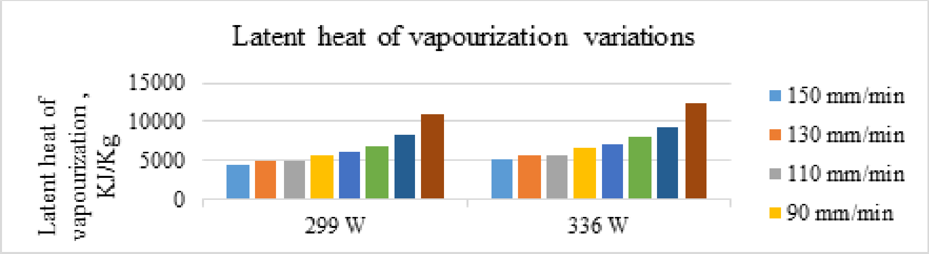

Graph 5. Comparative analysis of latent heat of vaporization for various input powers and scanning speeds.

HTEZ length and thereby enhance thermal stress relief, with analysis conducted in reference to the substrate, highlighting the pivotal role of substrate characteristics in the remanufacturing process.

Graphs 3 and 4 illustrate the expansion of zonal area as travel speed decreases for both 299W and 336W power settings. This observation suggests that greater beam interaction time leads to a larger area for stress relief. In the x-direction, the zonal area increased from 3.98 mm^2 to 14.52 mm^2 for 299W power, and from 4.71 mm^2 to 12.90 mm^2 for 336W power. Regarding the y-direction, the area expanded from 16.93 mm^2 to 61.13 mm^2 for 299W power, and from 18.8 mm^2 to 58.12 mm^2 for 336W power. Finally, in the z-direction, the zonal area increased from 6.27 mm^2 to 7.70 mm^2 for 299W power, and from 7.29 mm^2 to 6.21 mm^2 for 336W power. These findings indicate that prolonged beam interaction time results in a larger area for stress relief.

The zonal area in the y-direction surpasses that of the x- and z-directions due to the movement of the heat/plasma beam along the y-direction. In the x-direction, for instance, at 299W and 150 mm/min, the zonal area measures 3.98 mm^2; reducing the beam speed to 90 mm/min maintains a similar zonal area of 3.99 mm^2 (as illustrated in Table 4). Further reductions in speed result in increased zonal areas, with the area reaching 14.52 mm^2 at 10 mm/min beam speed for 299W power. Similarly, for 336W power, the zonal area at 150 mm/min is 4.71 mm^2, and it remains nearly constant at 5.71 mm^2 as the speed decreases to 90 mm/min. Further reductions lead to larger zonal areas, with the area reaching 12.9 mm^2 at 10 mm/min beam speed for 336W power.

In the y-direction, where the plasma beam moves, zonal areas are generally higher compared to other directions. An increase in area is observed as the beam speed drops below 90 mm/min. For instance, at 299W and 150 mm/min, the zonal area is 16.9 mm^2, increasing to 23.77 mm^2 at 90 mm/min, and further to 61.13 mm^2 at 10 mm/min. A similar trend is observed for 336W power, with the area increasing from 18.88 mm^2 at 150 mm/min to 21.3 mm^2 at 90 mm/min, and to 58.12 mm^2 at 10 mm/min. There is minimal fluctuation in zonal areas in the z-direction. To mitigate material loss due to high temperatures, it is recommended to maintain a plasma beam interaction speed of 90 mm/min, as indicated by computational analysis. This finding is corroborated by SEM images, where clear observations of the molten zone, Heat Transfer Expansion Zone (HTEZ), and Heat Affected Zone (HAZ) are made at 299W and 90 mm/min speed. Further reduction in speed (10 mm/min at 336W power) accentuates the molten zone, indicating increased material loss.

As illustrated in the aforementioned Graph 5, alterations in scanning speed and input power exhibit an impact on the latent heat of vaporization (Lv). Comparing the obtained Lv with the standard value for SS316L (6100 KJ/Kg) facilitates further analysis. For instance, at a scanning speed of 150 mm/min and an input power of 299W, the Lv measures 4361 KJ/Kg, below the standard 6100 KJ/Kg. Decreasing the scanning speed results in an increase in Lv: at 100 mm/min, Lv is 4814 KJ/Kg, and at 70 mm/min and 299W, Lv reaches 6227 KJ/Kg. Further reduction in scanning speed to 50 mm/min elevates Lv to 6919 KJ/Kg, surpassing the standard 6100 KJ/Kg, indicating material degradation. Thus, for 299W input power, maintaining a scanning speed above 70 mm/min is advisable to prevent Lv from exceeding the standard value. Similar trends are observed with an input power of 336W, where Lv is 5110 KJ/Kg at 150 mm/min. Reducing the scanning speed to 90 mm/min increases Lv to 6513 KJ/Kg, and further to 7173 KJ/Kg at 70 mm/min, again surpassing the standard value.

The simulation outcomes propose that refining processing parameters, including input power and scanning speed, according to the latent heat of vaporization value, could result in notable reductions in build time with minimal performance compromises. Moreover, additional investigation into the impact of powder layer thickness on mechanical characteristics is imperative to validate the feasibility of these time savings without sacrificing performance. This necessity arises from the manner in which powder layers are constructed, presenting opportunities for substantial reductions in build time.

4.1 Experimental Results

Through optimization of four input parameters, significant enhancements in the surface finish of a component were achieved. Experimental findings revealed that the most favorable surface morphology was attained with plasma power ranging from 299 to 336 W and scanning speeds between 50 and 90 mm/min. This parameter combination notably improved the component's surface finish. Inadequate remelting was observed when plasma power fell below 299 W or when the travel speed exceeded 90 mm/min. Utilizing a plasma power of 336 W resulted in a surface roughness of 5.456 μm Ra. Experiment 2 consistently yielded surface roughness values between 12 and 13 μm, indicating alignment with the outcomes. Despite efforts to utilize lower plasma power, achieving satisfactory surface flatness by melting peaks and filling valleys remained elusive. Ongoing efforts aim to identify more effective approaches to achieve the desired outcome.

In experiment 5, employing higher plasma power led to reduced surface roughness by effectively melting peaks and filling valleys, resulting in a smoother surface. Decreasing beam interaction time corresponded with an increase in the length of the Heat Transfer Element Zone (HTEZ) from 3.07 mm to 3.48 mm, accompanied by an increase in surface roughness from 13 to 18 μm. By employing optimal process parameters, surface roughness could surpass baseline PBR single-pass roughness by 60%. The use of SS316L PBR in additive manufacturing components holds potential for minimizing surface roughness. Future research will focus on multi-pass strategies to further decrease Ra, while an increase in surface microhardness was consistently observed across all trials.

The SEM image depicted in Figure 8 illustrates that elevated power and reduced beam interaction time yield an expanded molten zone. Nonetheless, this also leads to greater material loss due to increased zonal areas. Hence, meticulous consideration of power and beam interaction time is crucial when establishing process parameter values to mitigate excessive material loss.

5.0 Conclusion

This study presents the outcomes of both experimental and computational investigations focusing on the utilization of single-pass remelting to assess the effects of Plasma Beam Remelting (PBR) on conditioned SS316L surfaces. The analysis is conducted with respect to the substrate, emphasizing the significance of substrate properties in

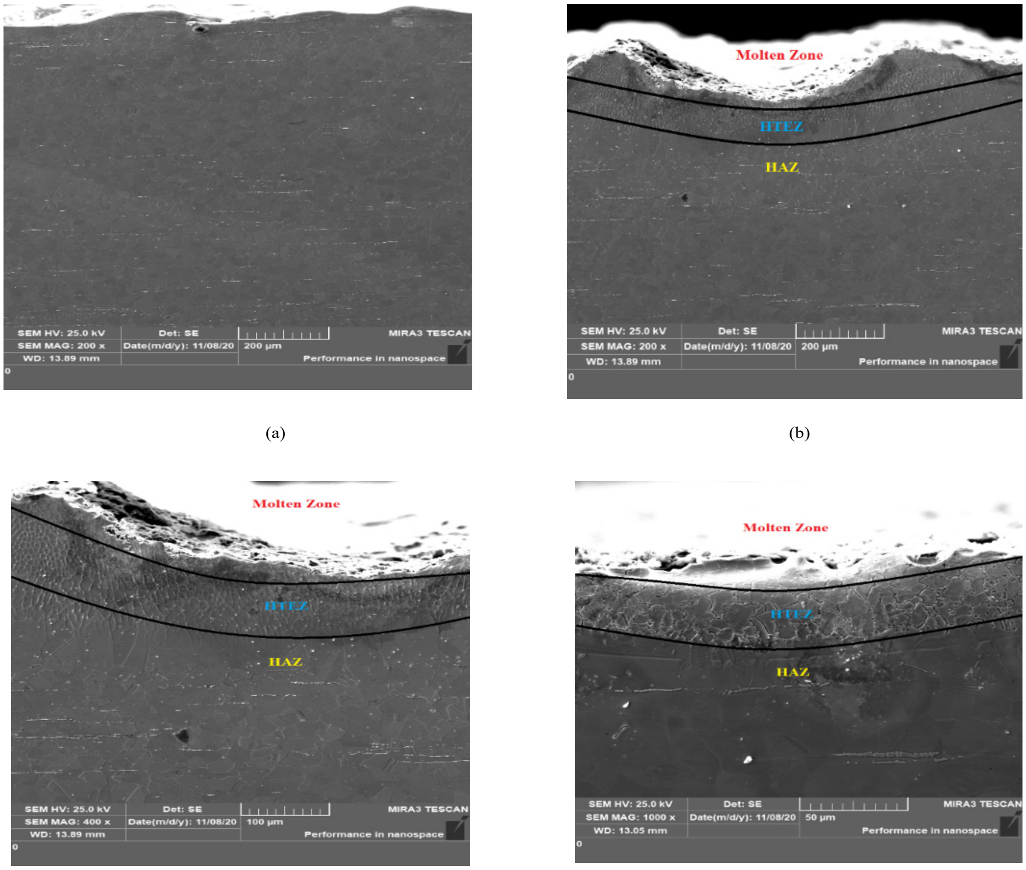

(a) (b) (c) (d)

Figure 8. SEM images of various trials: **(a)** Untreated sample **(b)** Sample: 299W power and 130mm/min travel speed **(c)** Sample: 299W power and 90mm/min travel speed **(d)** Sample: 336W power and 30mm/min travel speed

the remanufacturing process. The success of this approach underscores the viability of PBR as a feasible alternative to traditional surface enhancement methods such as laser and electron beam techniques. Drawing from the insights gleaned from this research, the following conclusions can be made: PBR serves as a dependable method for enhancing the surface characteristics of SS316L, enabling superior performance in applications requiring enhanced surface properties. Furthermore, the single-pass remelting process proves to be more efficient and cost-effective compared to conventional surface enhancement techniques, rendering it an optimal choice for numerous applications in remanufacturing scenarios.

1. Both the input power of the beam and its travel speed exert notable influence on the duration of the beam's interaction with materials.
2. Temperature-dependent fluctuations in thermal properties can be effectively modelled computationally, providing a richer set of information compared to conventional techniques.
3. In the x-direction, the zonal area measures 3.98 mm^2 for 299W power and a scanning speed of 150 mm/min; reducing the speed to 90 mm/min results in a negligible change, maintaining the area at approximately 3.99 mm^2. Further reduction in speed leads to an expansion of the zonal region. The optimal plasma beam interaction speed, determined computationally, is 90 mm/min.
4. Utilizing computational simulations offers advantages in terms of time, cost, and effort savings. Researchers may opt for a computational approach prior to conducting experiments to

forecast outcomes and mitigate the expenses associated with experimentation.

5. In order to attain a uniform and consistent surface, a specific minimum input energy and beam travel speed are necessary. In the present study, this value was determined to be 90 mm/min.
6. The length of the Heat Transfer Element Zone (HTEZ) increases proportionally with both the input power and beam interaction time. Furthermore, the zonal area in all three directions is influenced by both the input power and beam travel speed.

6.0 References

1. Wang S, Gu H, Wang W, Li C, Ren L, Wang Z, *et al.* Study on microstructural and mechanical properties of an Al-Cu-Sn alloy wall deposited by double-wire arc additive manufacturing process. Materials (Basel). 2020; 13(1). https://doi.org/10.3390/ma13010073 PMid:31877864 PMCid: PMC6981438
2. Ning J, Wang W, Ning X, Sievers DE, Garmestani H, Liang SY. Analytical thermal modelling of powder bed metal additive manufacturing considering powder size variation and packing. Materials (Basel). 2020; 13(8). https://doi.org/10.3390/ma13081988 PMid:32344571 PMCid: PMC7215875
3. Sun X, Zhang X, Xie Y. Surface defects in two-dimensional photocatalysts for efficient organic synthesis. Matter. 2020; 2(4):842-61. https://doi.org/10.1016/j.matt.2020.02.006
4. Rosa B, Hascoët JY, Mognol P. Topography modelling of laser polishing on AISI 316L milled surfaces. Mech Ind. 2014; 15(1):51-61. https://doi.org/10.1051/meca/2014003
5. Xiao J, Huang W, Li T, Wu Y, Chen X, Zhang J, *et al.* Laser-assisted surface conditioning of a residual pattern on single crystal silicon induced by ultra-precision cutting. Opt Mater Express. 2022; 12(4):1303. https://doi.org/10.1364/OME.453263
6. Jhavar S, Jain NK, Paul CP. Development of micro-plasma transferred arc (μ-PTA) wire deposition process for additive layer manufacturing applications. J Mater Process Technol. 2014; 214(5):1102-10. https://doi.org/10.1016/j.jmatprotec.2013.12.016
7. Denlinger ER, Irwin J, Michaleris P. Thermomechanical modelling of additive manufacturing large parts. J Manuf Sci Eng Trans ASME. 2014; 136(6):1-8. https://doi.org/10.1115/1.4028669
8. Teimouri R, Sohrabpoor H, Grabowski M, Wyszyński D, Skoczypiec S, Raghavendra R. Simulation of surface roughness evolution of additively manufactured material fabricated by laser powder bed fusion and post-processed by burnishing. J Manuf Process. 2022; 84(October):10-27. https://doi.org/10.1016/j.jmapro.2022.09.045
9. Zheng B, Trofimov V, Yang Y, Liu L, Feng Y, Zheng Z, *et al.* Study on additive and subtractive manufacturing of high-quality surface parts enabled by picosecond laser. J Mater Process Technol. 2023; 318(May). https://doi.org/10.1016/j.jmatprotec.2023.118013
10. Chari VS, Jhavar S. Surface properties modification of SS316L using Plasma Beam Remelting (PBR) and its applications in additive manufacturing. Trans Indian Natl Acad Eng. 2021; 6(4):1017-25. https://doi.org/10.1007/s41403-021-00237-8
11. Vykhtar B, Lingner M, Richter AM, Hoops F. Monitoring and local gas shielding at laser-based welding of titanium alloys. Procedia CIRP. 2022; 111:532-5. https://doi.org/10.1016/j.procir.2022.08.085
12. Saprykin AA, Ibragimov EA, Babakova E V. Modeling the temperature fields of copper powder melting in the process of selective laser melting. IOP Conf Ser Mater Sci Eng. 2016; 142(1). https://doi.org/10.1088/1757-899X/142/1/012061
13. Rubio-Ramirez C, Giarollo DF, Mazzaferro JE, Mazzaferro CP. Prediction of angular distortion due to GMAW process of thin-sheets Hardox 450® steel by numerical model and artificial neural network. J Manuf Process. 2021; 68(PA):1202-13. https://doi.org/10.1016/j.jmapro.2021.06.045
14. Sloderbach Z, Pajak J. Determination of ranges of components of heat affected zone including changes of structure. Arch Metall Mater. 2015; 60(4):2607-12. https://doi.org/10.1515/amm-2015-0421